Extending Electrochemical Aptamer-Based Sensing to Microfabricated Sensor Formats

Christopher E. Larson, Emmanuel Ramirez, Chelsea N. Brown, Kayla Wang, Tod Kippin, Kevin Plaxco, and Ellis Meng, *Fellow, IEEE*

***Abstract*—Electrochemical aptamer-based (EAB) sensing is a generalizable approach to monitoring a wide range of molecular targets. Selective, dynamically responsive, real-time measurements are possible in complex body fluids while using standard electrochemical methods for read out. To advance miniaturized, wearable EAB sensing formats, 17 candidate materials compatible with microfabrication into 2D and 3D microstructures were investigated as sensor substrates. Since the aptamer attachment chemistry requires a gold surface, adhesion of gold thin films was evaluated followed by compatibility with EAB surface functionalization chemistry and the electrochemical interrogation method. Sensing results for each material were benchmarked against the gold standard solid gold microwire sensor format. Finally, two microneedle-based EAB sensor formats were demonstrated at the benchtop and *in vivo*, by modifying commercially produced microneedles and developing a novel laser-machined polyether ether ketone (PEEK) microneedle array. Multiplexed sensing was enabled by selective functionalization of subgroups of needles within a single array. [2025-0204]**

***Index Terms*—Aptamers, laser micromachining, electrochemical sensors, microneedles, wearable sensors.**

I. Introduction

NEW measurement technologies enable advances in healthcare by providing access to new categories of physiological information, or by making strides in accuracy, precision, timeliness, and convenience. A frontier poised for impact is the real-time sensing of biomolecules performed in or on the body which promises dynamic response to targeted molecules. In contrast, many current techniques have an inherent delay in generating useable data due to reliance on sample collection and benchtop analyses.

Sensors providing real-time, actionable data about molecular concentrations may play a key role in future management of diseases, therapeutic drug monitoring, feedback-controlled drug delivery, precision medicine, physical performance enhancement, general health or diagnostic monitoring, and basic biological research [1], [2], [3], [4], [5], [6], [7], [8], [9]. Methods to measure molecular concentrations in or on the body can be characterized by the bioreceptor (*e.g.*, enzyme, antibody, or nucleic acid) and transduction mechanism (*e.g.*, electrochemical, mechanical, optical, or other) employed [10].

The gold standard in this sensor category is the wearable continuous glucose monitor (CGM), with a sensor filament penetrating ~5 mm into the fatty tissues below the skin. CGMs provide an electrochemical current reading indicative of glucose concentration by detecting biproducts of its breakdown by glucose oxidase. Commercial CGMs benefit more than 9 million users worldwide [11], however the enzyme-based methods are inherently limited to targets with enzymatic reactivity.

Antibodies can be produced for a wide range of targets and methods to transduce the bound antibodies include surface plasmon resonance, quartz crystal microbalances, or field effect transistors. However, antibodies are generally slow to dissociate from their targets, limiting their applicability to real-time tracking [12] and, without strategic precautions, transduction methods tend to suffer from signal contributed by non-specific adsorption of proteins which cannot be distinguished from target binding [13], [14].

Aptamers are short, synthetic, single-stranded chains of nucleic acids (*e.g.*, DNA or RNA) engineered to bind a target molecule by a process of "exponential enrichment;" a high affinity aptamer is obtained via systematic evolution of ligands by exponential enrichment (SELEX)—an iterative process involving ~ 10^{15} randomly sequenced strands which are progressively selected, amplified, and enriched [15]. This development process removes most constraints that would limit potential target molecules. Aptamers have been demonstrated as bioreceptors against a wide range of targets including antibiotics, chemotherapeutics, drugs of abuse, protein metabolites, and biomarkers [2], [5], [16]. Furthermore, this engineered nature of aptamers offers potential for continual improvement of functional characteristics such as affinity and selectivity. As a result, aptamer-based sensing has

Received 24 October 2025; revised 12 January 2026; accepted 24 February 2026. Date of publication 16 March 2026; date of current version 4 June 2026. This work was supported in part by the Office of Naval Research under Award N00014-20-1-2164 and Award N00014-21-1-2447. Subject Editor S. Rajaraman. *(Corresponding author: Ellis Meng.)*

Christopher E. Larson and Emmanuel Ramirez are with the Alfred E. Mann Department of Biomedical Engineering, University of Southern California, Los Angeles, CA 90089 USA (e-mail: larsonce@usc.edu; er88866@usc.edu).

Chelsea N. Brown is with the Institute of Collaborative Biotechnologies, University of California, Santa Barbara, Santa Barbara, CA 93106 USA (e-mail: cnbrown@ucsb.edu).

Kayla Wang and Tod Kippin are with the Department of Psychological and Brain Sciences, University of California, Santa Barbara, Santa Barbara, CA 93106 USA (e-mail: ywang666@ucsb.edu; kippin@ucsb.edu).

Kevin Plaxco is with the Department of Chemistry and Biochemistry, University of California, Santa Barbara, Santa Barbara, CA 93106 USA (e-mail: kwp@chem.ucsb.edu).

Ellis Meng is with the Alfred E. Mann Department of Biomedical Engineering and the Ming Hsieh Department of Electrical and Computer Engineering, University of Southern California, Los Angeles, CA 90089 USA (e-mail: ellis.meng@usc.edu).

This article has supplementary downloadable material available at https://doi.org/10.1109/JMEMS.2026.3669363, provided by the authors.

Digital Object Identifier 10.1109/JMEMS.2026.3669363

1057-7157 © 2026 IEEE. All rights reserved, including rights for text and data mining, and training of artificial intelligence and similar technologies. Personal use is permitted, but republication/redistribution requires IEEE permission.
See https://www.ieee.org/publications/rights/index.html for more information.

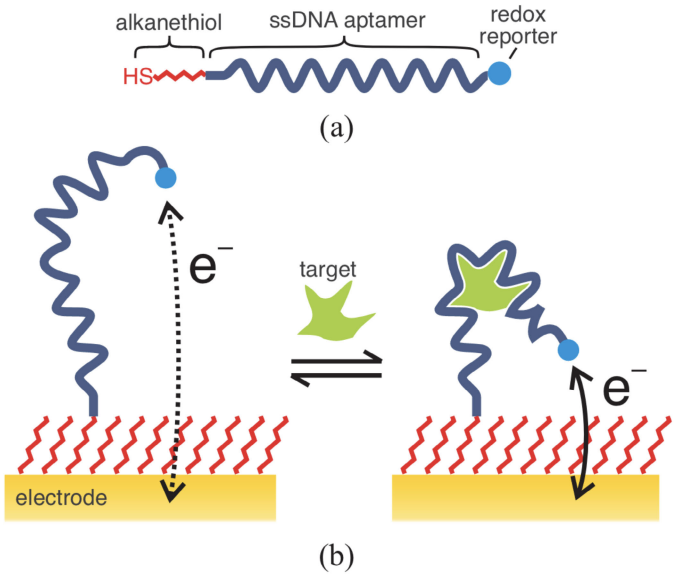


Fig. 1. EAB sensing concept. (a) Modified aptamer construct with alkanethiol on one end and redox reporter on the other. (b) Illustration of detection scheme. Aptamer binding to target affects kinetics of electron transfer between the redox reporter and the electrode surface and is read out electrochemically.

TABLE I
MATERIALS EVALUATED AS SUBSTRATES FOR EAB SENSORS

Category	Material
Common Microfabrication Materials	Soda Lime Glass
	Silicon
	PECVD SiO_2 (on silicon wafer)
	316L Stainless Steel
	Parylene C (on glass and stainless steel)
Thermoplastic Polymers	Polymethyl Methacrylate (PMMA)
	Polyether Ether Ketone (PEEK)
	Polyetherimide (PEI, Ultem)
	Cyclic Olefin Copolymer (COC)
	Polystyrene
	MT1300 Liquid Crystal Polymer (LCP)
	MT4310 LCP
	MT4350 LCP
	FIT30 LCP
SLA Resins	HTL
	HT200
	BIO

performed with excellent selectivity in complex body fluids, *i.e.*, whole blood [5]. Aptamer-target binding is reversible with average dissociation constants faster than those of antibodies by more than two orders of magnitude, enabling continuous real-time tracking of rising and falling target concentrations [12].

Transduction is conveniently achievable via electrochemical sensing. Aptamers are engineered to undergo a conformational change, *i.e.*, folding upon binding to the target molecule. By immobilizing one end of the aptamer on the electrode surface and attaching a redox reporter (*e.g.*, methylene blue) to the other end, binding-induced folding moves the redox reporter closer to the electrode, affecting the kinetics of electron transfer and producing an electrochemically detectable response (Fig. 1) [16]. Standard electrochemical techniques such as square wave voltammetry (SWV) can be used to interrogate the proportion of bound and unbound aptamers on an electrode surface via differences in electron transfer and thereby readout the concentration of a specific target. Wearable miniaturized potentiostats [17] further enable in- and on-body electrochemical aptamer-based (EAB) sensing.

This approach was introduced in 2005 as EAB sensing using a disk electrode format [18]. A microwire format enabled monitoring in blood vessels, brain ventricles, and solid tumors, and more recently, microfluidic chip and thin film polymer formats were introduced [5], [19], [20], [21]. While surgical placement is commonly required, there is interest in expanding EAB sensing to minimally invasive formats monitoring just below or within the skin to realize its broad potential, leading to the exploration of microneedle-based EAB sensors [22], [23], [24].

Preparation of EAB sensors requires immobilization of the aptamer onto an electrode, usually by chemisorption of thiols to Au [25]. Packing of the surface between the modified aptamers with additional alkanethiols orients the aptamers upright and prevents non-specific interactions of the aptamers with the Au electrode, resulting in more uniform binding and folding functionality (Fig. S1) [25]. Graphene, carbon nanotubes, and other carbon-based electrodes have been explored as potential alternatives [25], [26], [27], [28], [29], however Au is preferred for its inertness and ability to support formation of dense and well-ordered monolayers [25].

We seek to adapt EAB sensors to novel formats for in- and on-body EAB sensing by investigating substrate materials supporting robust adhesion to deposited Au thin films and compatibility with aptamer self-assembly processes. Candidate materials were also selected based on their ability to form 2D and 3D structures suitable for sensor interfaces. Using test coupons, Au film adhesion was evaluated and EAB sensing capability benchmarked against Au microwire using vancomycin as a model molecule. Substrates exhibiting excellent adhesion were used to modify commercial microneedles into EAB sensor prototypes and realize a novel polymer-substrate microneedle EAB sensing array. Microneedle-format EAB sensing was demonstrated at the benchtop and *in vivo*, along with a method to selectively functionalize groups of microneedles.

II. METHODS

A. Substrate Material Selection and Sample Preparation

The standard format for EAB sensors is a solid Au wire; this is used here as a control. We selected, based on literature search and to the best of our knowledge, 17 materials onto which (1) Au could be thermally evaporated and (2) prioritized biocompatibility, mechanical robustness, machinability, and potential compatibility with chemicals used in EAB functionalization. After considering criteria related to

material properties, considerations around machinability led to the selection of materials compatible with microfabrication followed by thermoplastics and stereolithography (SLA) resins (3D-printable photopolymers) that have not been traditionally used in microfabrication (Table I).

The wire electrode controls were made by soldering 45 mm long, 200 μm diameter solid Au wires (99.9% purity, ThermoFisher Scientific, Waltham, MA) to Au-plated connector pins (CH Instruments, Austin, TX) and insulating all but the last 6 mm with polyolefin heat-shrink tubing (McMaster-Carr, Elmhurst, IL).

For adhesion testing, planar coupons were prepared from the candidate materials (approximately 25×75 mm) as described in Supplementary Material. The coupons were cleaned, dehydrated, then coated with a 10 nm Ti adhesion layer and 100 nm Au by e-beam evaporation.

1) Adhesion Testing: A cross-cut tape test was used to evaluate metal-substrate adhesion in close alignment with ASTM D3359-B [30]. Using a fresh X-Acto blade and a laser-machined acrylic guide, 11 cuts measuring 20 mm long and at a pitch of 1 mm were made through the Ti/Au layer, then the guide was turned 90° and 11 more cuts made. Scotch Tape 600 (3M, St. Paul, MN) was applied and rubbed to remove air bubbles, rested for 60 s, and the tape rapidly pulled off at an angle close to 180°. Adhesion ratings from 0 (poor) to 5 (excellent) were assigned based on the percentage of metal removed by the tape as determined by visual inspection, using a microscope when necessary, and further verified using ImageJ software.

2) EAB Sensing Compatibility: To examine compatibility with EAB surface functionalization, Ti/Au coated coupons measuring 4×40 mm^2 were prepared from substrate materials (three each) that passed the adhesion testing with no Au removed. To match the geometric surface area of the 200 μm $\times$ 6 mm Au wire electrode, coupons were masked with polyimide tape defined by a 35 watt Epilog Helix CO_2 laser (Golden, CO) to expose a 2.2 mm diameter (3.8 mm^2) area (Fig. S2a). The opposite end of each coupon was fully exposed, allowing electrical connection via alligator clip.

Vancomycin- and phenylalanine-targeting aptamers were purchased from Integrated DNA Technologies (Coralville, IA) (sequences in Table SI). $MgCl_2$, H_2SO_4, tris(2-carboxyethyl) phosphine (TCEP) and 6-mercapto-1-hexanol (MCH) were purchased from Sigma Aldrich (St. Louis, MO). Phosphate-buffered saline (PBS) was purchased from VWR (Radnor, PA).

Immediately prior to functionalization, all electrodes were electrochemically cleaned in 0.05 M H_2SO_4 using a Gamry Reference 600 potentiostat, aqueous Ag/AgCl reference electrode (RE), and 0.1 cm^2 Pt counter electrode (CE). 1.4 V DC was applied for 60 seconds followed by 15 cycles of cyclic voltammetry from -1.0 to + 1.3 V at 0.1 V/s [31], [32].

Functionalization involved generating an aptamer self-assembled monolayer along with MCH backfilling on Au [33], [34]. 100 μM aptamer solution was prepared for Au conjugation by incubating at room temperature for at least one hour in an excess of TCEP. The aptamer was then diluted to 500 nM in 1$\times$ PBS. Electrodes were triple rinsed in deionized water and incubated in the aptamer solution for one hour. Next, the electrodes were incubated in 10 mM MCH in 1$\times$ PBS overnight to complete monolayer coverage of the Au. Samples and solutions were stored in the dark during all steps.

Voltammetric titration was conducted to observe the signal response of each sensor. With an aqueous Ag/AgCl RE and Pt wire CE, sensors were evaluated in room temperature 1$\times$ PBS with 2 mM $MgCl_2$ and vancomycin concentration was increased from 1 μM to 1 mM (Fig. S2b). SWV was performed at each concentration, including a no-target measurement, using a Gamry Reference 600 potentiostat (100 Hz from -0.1 to -0.4 V with amplitude 25 mV and step size 1 mV). SWV involved application of a square potential waveform superimposed on a stairstep pattern; subtraction of reverse current from forward current sampled at each step yielded a difference current, I_{dif}. Successful functionalization resulted in an obvious peak in I_{dif} at approximately -0.3 V which increased in amplitude with concentration. Using a custom Python script, signal gain was calculated as a ratio of the peak amplitude at each concentration to that with no target present. To negate the effects of noise and background current on the signal gain calculation, the script first smoothed each voltammogram via moving average filter of 11 points (point spacing determined by the voltage step size), and each baseline was adjusted to zero by subtracting a linear set of values defined by local minima adjacent to each side of the peak. To represent 0 μM measurements on the same logarithmic scale as the other concentrations, they were plotted at a value of $10^{-7}\mu$M and the axis label at that point was manually changed to 0.

B. Microneedle Arrays

Of the materials that passed both the metal adhesion and EAB compatibility tests, we selected two to allow demonstration of different approaches to a microneedle sensing interface: a coating over a supporting backbone, or as the substrate in which the microneedle is directly machined. For the first approach, Parylene C was selected as it can be vapor deposited as a conformal coating over any surface. This enabled coating of commercially produced microneedle substrates: a high-resolution 3D printed SLA MNA and an off-the-shelf stainless steel (SS) MNA.

For the second approach, PEEK is available in thin sheets and can be precisely machined via laser micro-machining to form needle structures. The material can also be bent out-of-plane to achieve a "patch" configuration of arrayed microneedles.

1) MNA Fabrication:

a) SLA resin MNA: We designed MNAs for stereolithography having 48 solid microneedles in four groups of 12. Each conical microneedle was 800 μm high and had a base diameter of 300 μm, corresponding to a surface area of 0.38 mm^2 (or 18.4 mm^2 for all 48). A temporary frame was designed for handling during post-processing steps, after which the MNAs were released.

The design was printed in HTL resin by Boston Micro Fabrication (Maynard, MA) with 2 μm *x-y* resolution (Fig. 2a). Printed MNAs were conformally coated in 4 μm of Parylene C. Notches in the surrounding frame allowed positioning

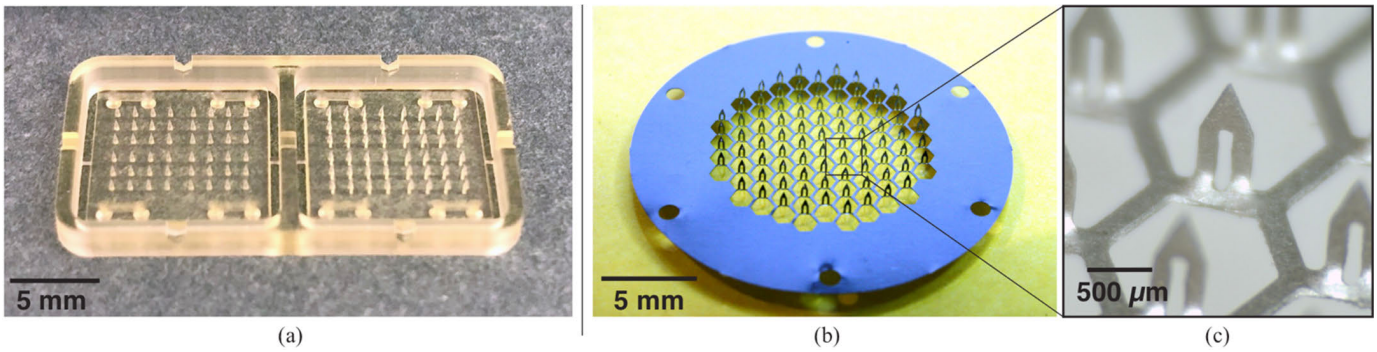


Fig. 2. Commercially produced microneedle structures prior to modification for EAB sensing. (a) A pair of SLA MNAs with a surrounding frame for handling and shadow mask alignment. (b) AdminPatch 900 stainless steel drug delivery microneedle array from AdminMed [35] and (c) a magnified view of its cut-out and bent microneedles.

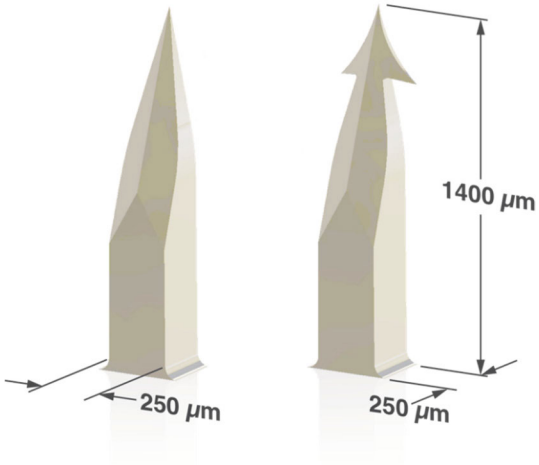


Fig. 3. CAD renderings of the straight (left) and barbed (right) microneedle designs fabricated by laser machining PEEK.

of wires acting as a shadow mask and defining four distinct microneedle sensors. Following oxygen plasma cleaning (300 s, 100 W, 125 mTorr, 30 sccm O_2, YES-CV200RFS), 10/100 nm of Ti/Au was deposited via e-beam evaporation. Through-holes in the substrate were used to route electrical leads to the back of the MNA, and trenches extending from the holes allowed each lead to lie flat and be connected to the Au surface using silver epoxy (Fig. S3).

b) Stainless steel MNA: AdminPatch 900 stainless steel MNAs intended for drug delivery applications were purchased from AdminMed (Sunnyvale, CA) and modified for EAB sensing. The devices included 85 out-of-plane, hexagonally-arrayed microneedles in a 70 μm thick and 20 mm diameter stainless steel sheet, each 800 μm tall (Fig. 2b). Total single-sided surface area was 26 mm^2. The modification process is detailed in Supplementary Material (Fig. S4). The stainless steel frame was passivated by conformal Parylene C coating (4 μm), Ti/Au deposited, and non-sensing margins insulated with marine epoxy (Loctite, Rocky Hill, CT).

c) Laser-machined polymer MNA: We designed laser machined MNAs (32 microneedles in 250 μm thick PEEK sheets distributed across a 10×10 mm^2 area in seven staggered rows). A 5.5 $\times$ 2.5 mm^2 connector tab was added on one edge for a total footprint of 12×14 mm^2 including margins. Microneedles were 1400 μm long and 250 μm wide with a 30° tip. The length was informed by preliminary experiments on rat skin. To improve retention in the skin, a second tip design with a barb on each side (300 μm from the point and extending out 100 μm from the edge) was investigated (Fig. 3). Single-sided surface area was 0.27 mm^2 for each microneedle and 8.6 mm^2 for the array. For mechanical testing, devices having one to seven in-plane microneedles on the edge of a 10 mm square sheet with two holes for bolting to a testing fixture were used.

PEEK MNA sensor fabrication (Fig. 4) is detailed in Supplementary Material. Briefly, PEEK MNAs were machined using a 515 nm femtosecond laser, galvo scanner, and pneumatically controlled stage in an integrated laser micromachining system (Optec Laser Systems, San Diego, CA). Microneedle outlines were laser cut as pointed cantilevers in oval windows. The tips were laser beveled by mounting at an angle. All microneedles were simultaneously bent out-of-plane by aligning and clamping the cut sheets between a custom jig (Fig. S5a) and a rubber sheet. After cleaning, a laser-cut shadow mask was used with Ti/Au deposition to define five groups of microneedles and contact pads as independent electrodes. Two insulation methods were examined: application of laser-cut polyimide tape and conformal coating with Parylene C while microneedle tips were protected in an elastomeric sheet.

The PEEK substrate thickness allowed the five MNA contact pads to be directly mated to a 10 position zero-insertion force (ZIF) connector (Molex 5034801000, DigiKey, Thief River Falls, MN) soldered onto a flat flexible cable (FFC) (Molex 151660095, DigiKey). Each MNA contact pad was addressed by two pins within the ZIF connector for redundancy.

d) Custom vessels for incubating microneedles: To functionalize MNAs, custom incubation micro-vessels were fabricated using two sheets of 1.59 mm thick acrylic joined with epoxy. For the AdminPatch MNAs, the first sheet was laser cut to create a circular opening 12.5 mm in diameter, then joined to a solid sheet, resulting in a shallow dish (~ 200 μL). A similar vessel was made for the SLA MNAs.

To selectively apply different aptamers to different needles for multiplexed sensing, an incubation fixture was developed

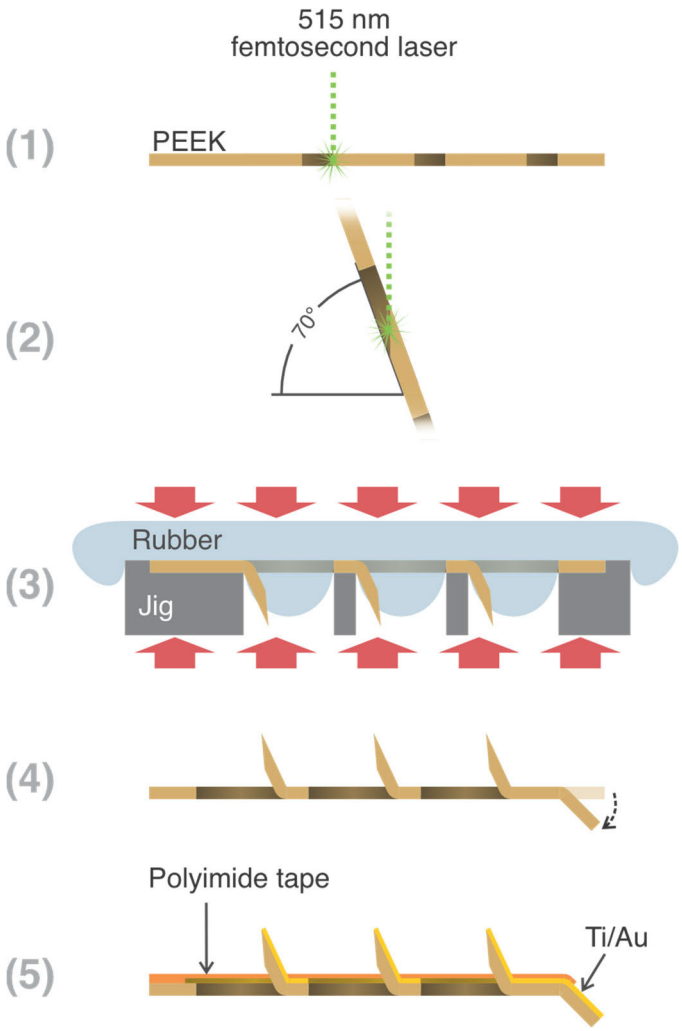


Fig. 4. Fabrication process for PEEK MNAs. (1) Laser machine microneedle outlines. (2) Laser bevel microneedle tips by mounting at 70°. (3) Bend microneedles out-of-plane by compression with a rubber sheet into a laser-machined jig. (4) Bend connection tab. (5) Deposit Ti/Au via e-beam evaporation through a shadow mask (not shown) and insulate Au traces via laser-cut polyimide tape (shown) or conformal Parylene C coating (not shown).

for the PEEK MNA to accommodate two working electrodes (WE), two counter electrodes (CE) and one shared reference electrode (RE). This fixture used PDMS (Sylgard 184, Dow, Midland, MI) cast from a mold SLA printed with CADworks3D Master Mold for PDMS resin (Concord, Ontario, Canada) to define separate incubation compartments for each WE (~ 25 μL volume). The mold was conditioned with three cycles of PDMS casting, curing, and cleaning with isopropanol, after which the casted PDMS parts released reliably. PEEK or steel tubing were inserted laterally into each compartment, providing fluidic access (Fig. S9). PEEK MNAs were loaded onto the PDMS incubation fixture, aligning the WE electrode groups with the compartments, and a silicone sheet placed over top of the array. Acrylic plates sandwiched the assembly and applied pressure to the stack with screws, sealing the microfluidic compartments to the MNA. Solution was sequentially injected into each compartment, following the surface functionalization protocol previously described. To change solution, 400 μL of the next solution was applied to the compartment based on visual calibration using dyed water. Alternatively, all microneedles could be functionalized as a single WE by preloading solution into all five compartments (~ 80 μL total).

2) MNA Characterization:

a) Mechanical: We confirmed MNAs could be inserted into a skin model. For the PEEK MNAs, we measured buckling, insertion, and retention forces. Porcine ear was selected for its similarity to human skin [35]. Each MNA was pressed into the skin by finger, held for ~5 s, and then removed. Microneedle punctures were observed under optical microscope.

Force measurements were collected using a stepper motor (ThorLabs DRV250, Newton, NJ), load cell (Futek LSB201, QSH02033, Irvine, CA), and SLA-printed block to which the microneedles were mounted (Fig. S10). A LabVIEW script and DAQ interface (National Instruments, Austin, TX) collected load cell measurements (100 samples/s). To measure buckling force, in-plane single PEEK microneedles were mounted and advanced into an aluminum block (0.03 mm/s). Buckling force was the maximum force produced just before the needle bent against the block. To measure insertion and retention force, single PEEK microneedles were advanced (0.03 mm/s) into porcine skin securely held by a frame. The motor was paused for ~10 s upon full insertion, then retracted at the same speed. Insertion force was the force at which an observable slip, or brief drop in force, first occurred. Retention force was the greatest tensile force achieved just before the microneedle disengaged from the skin.

b) In vitro sensing: MNAs were electrochemically cleaned and functionalized, following the described protocols, for detection of vancomycin or phenylalanine. Functionalized MNAs were connected to a CH Instruments 1030C multichannel potentiostat and placed with aqueous Ag/AgCl RE and Pt wire CE into a beaker of 1× PBS and 2 mM $MgCl_2$ at room temperature. Voltammetric titration was performed across a range of concentrations up to 1 mM. SWV was applied at 100 Hz for vancomycin sensors and 300 Hz for phenylalanine sensors; these frequencies were identified during calibration as yielding a strong signal gain for each aptamer. Voltammograms were processed, including smoothing, baseline adjustment, and signal gain calculation.

c) In vivo sensing: We performed subcutaneous and intracutaneous *in vivo* measurements with PEEK MNA EAB sensors on anesthetized adult (4-6 months old) male (300-500 g) Sprague-Dawley rats. *In vivo* studies were performed under the procedures outlined by the Guidance for the Care and Use of Laboratory Animals, approved by the University of California, Santa Barbara Institutional Animal Care and Use Committee. Detailed methods are provided in Supplementary Material. In the first experiment, an MNA was placed subcutaneously and compared to an in-vein Au wire control. After ~40 min to establish a baseline, 30 mg/kg vancomycin was infused intravenously over 1 min and measurements were collected for another ~2 hr. In the second experiment, a PEEK MNA was inserted into the skin and compared to a subcutaneous Au wire control. After waiting

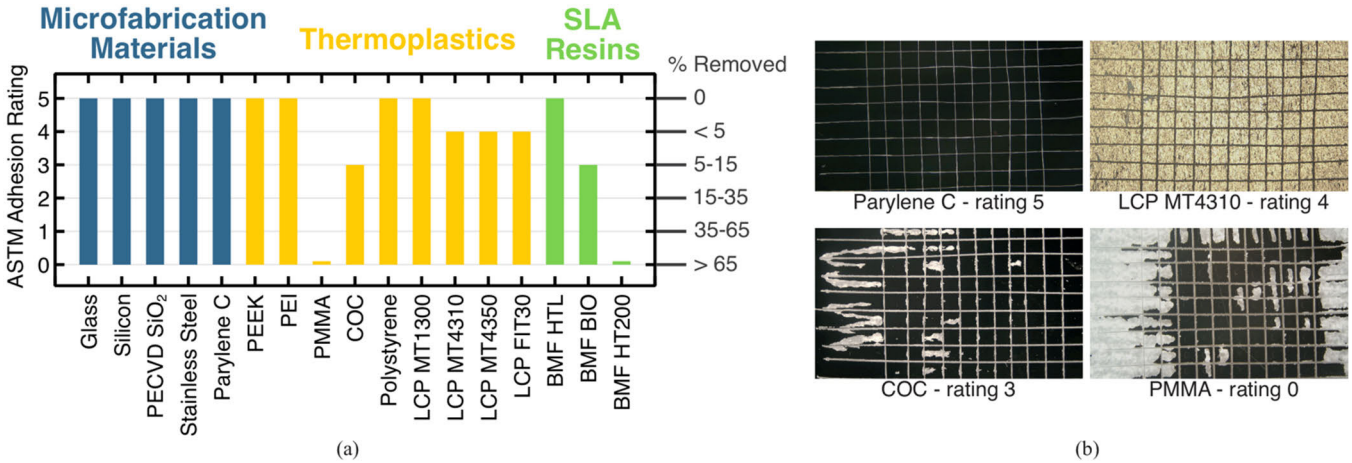


Fig. 5. (a) Ti/Au adhesion ratings assessed using cross-cut tape test. (b) Representative images of each rating from the cross-cut tape test. Au appears black due to backlighting. Grid spacing is 1 mm.

~35 min to establish a baseline, 60 mg/kg vancomycin was infused intravenously over 1 min, and measurements were collected for another ~2.5 hr.

A Python script analyzed the voltammograms and performed smoothing and baseline adjustment as previously described. In addition to signal gain, kinetic differential measurement (KDM) was used for drift correction. 100 Hz was experimentally identified as an "on" frequency (associated peak amplitude increased with concentration), while 30 and 10 Hz behaved as "off" frequencies (peaks decreased). For each time point, the KDM value was calculated as the difference in gain at each frequency over their average:

$$KDM = \frac{\left(\frac{I_{on}}{I_{on,0}} - \frac{I_{off}}{I_{off,0}}\right)}{\frac{1}{2}\left(\frac{I_{on}}{I_{on,0}} + \frac{I_{off}}{I_{off,0}}\right)}$$

III. Results

A. Material Characterization

1) Adhesion: Following the cross-cut tape test, ten materials exhibited excellent adhesion with no Au removal observed (Fig. 5a). All other materials exhibited differing degrees of adhesive failure, with up to 80% Au removal (Fig. 5b). Results were consistent across three trials for each material. Materials with the highest adhesion rating (5 or 0% Au removed) were advanced.

2) EAB Compatibility: Three materials were eliminated from further consideration after failing EAB compatibility testing. Metal delaminated from the HTL samples during electrochemical cleaning in H_2SO_4. Sensors fabricated on stainless steel and uninsulated silicon substrates yielded no discernible peak. Seven materials yielded EAB sensors that produced strong electrochemical peaks (Fig. 6a) and responded to target with signal changes comparable to those for Au wire controls (Fig. 6b).

B. MNA Fabrication

AdminPatch stainless steel and SLA resin MNAs were coated with Parylene and Ti/Au (Fig. 7a, b), though only the modified AdminPatch MNAs could be functionalized.

For SLA MNAs, the surrounding frame simplified handling and the wire shadow mask was effective. The sloped surface of the SLA microneedles possessed a ridged, stair-step surface texture attributed to the discretely cured layers. Electrical continuity across the microneedle surfaces was not achieved after Ti/Au deposition, and inspection under microscope confirmed discontinuous Au film over the stepped surface (Fig. S11). This prevented further development of SLA MNAs in the current study, though the discontinuity issue may be solved with other approaches in future work.

The PEEK laser-machining resulted in sharp multi-electrode MNAs, however, mounting microneedles at 70° yielded a tip bevel angle of 30° rather than 20° due to the resulting tapered (non-vertical) sidewall profile. Scanning electron microscopy (SEM) images of the sharpened microneedles (Fig. S12) show a tip radius of 11 μm. In barbed microneedles, sharpening tapered and shortened the barbs to ~ 50 μm. Consequently, slight misalignment under the laser could result in an asymmetrical profile. The barbed microneedle maintained a tip radius similar to the non-barbed version but the tip angle deviated (60° instead of 30°).

Bending PEEK microneedles out-of-plane by clamping against a neoprene sheet consistently yielded an angle of 65° ± 2° (S.D., n = 6). Clamping against a harder silicone sheet could achieve larger angles up to 80°, but the silicone tended to tear and leave remnants in the microneedle windows, the removal of which risked damaging microneedles.

Abrasive slurries considered for ultrasonic removal of laser machining debris included 0.3 μm alumina slurry (Electron Microscopy Sciences, Hatfield, PA), Bar Keeper's Friend Cleanser (Indianapolis, IN), and pumice-based hand cleaner (Gojo Industries, Akron, OH). The pumice cleaner was most effective (12 hour cleaning) and microneedle tips were oriented upward to avoid blunting by abrasion against the bottom of the beaker.

Laser-cut polyimide tape insulation was effective and easily implemented (Fig. S7). Parylene insulation achieved well-defined sensing areas localized to the microneedle tips (Fig. S8). Approximately 400 μm of each microneedle shank

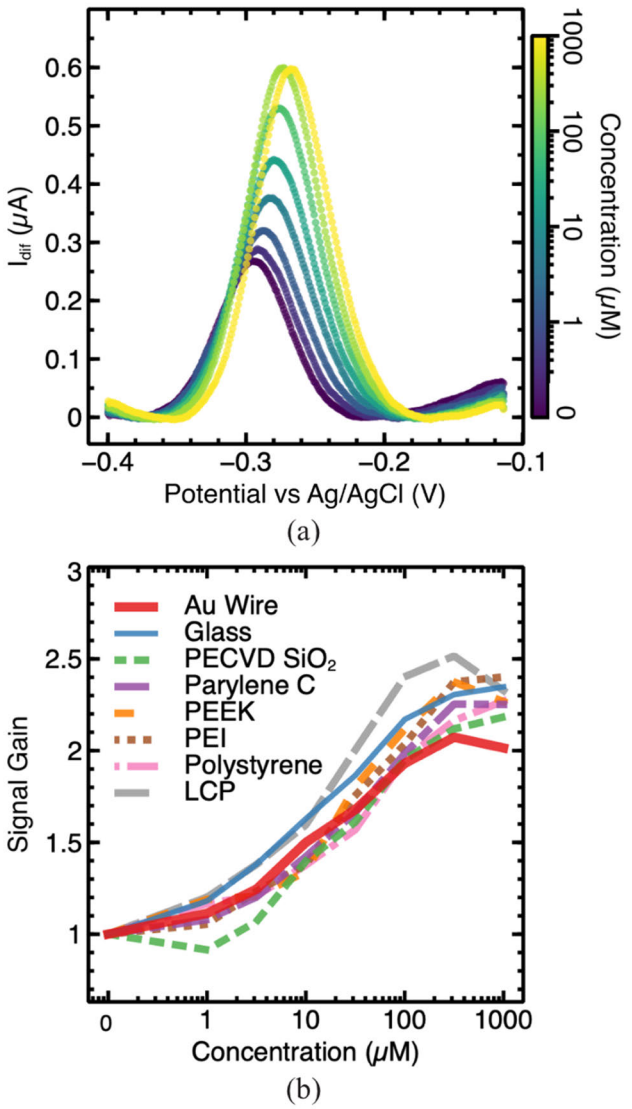


Fig. 6. (a) Representative set of SWV peaks in response to vancomycin (on Parylene C substrate). (b) Comparison of average signal gain for EAB sensors made on compatible substrates with the Au wire as a control (n= 3).

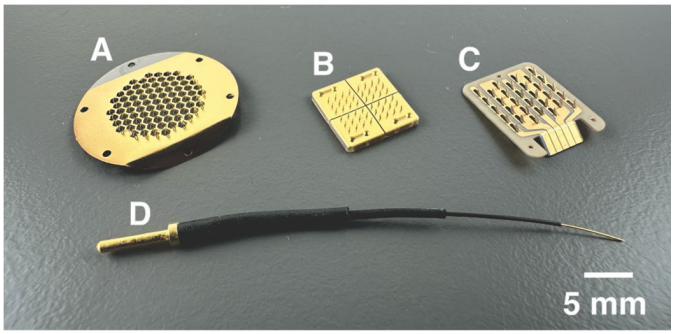


Fig. 7. Au-coated MNAs: (A) Single-electrode AdminPatch, (B) four-electrode SLA MNA, and (C) five-electrode PEEK MNA. (D) 200 μm solid Au wire sensor used as benchmark for *in vitro* studies (left: connector pin, right: sensor).

was insulated, resulting in a single-sided sensing area of ~0.15 mm^2.

Microneedle length after fabrication was ~ 1300 μm, with shortening attributed to laser kerf and position of the bending angle. Accounting for final dimensions, insulation, and bending angle, the depth spanned by the microneedle's sensing surface was about 360 to 1200 μm from the substrate.

TABLE II
INSERTION AND RETENTION FORCE MEASURED WITH SINGLE MICRONEEDLES AND SEVEN-MICRONEEDLE 1D ARRAYS OF BOTH STRAIGHT AND BARBED TIP DESIGNS IN PORCINE EAR

# of Microneedles	Tip	n	Insertion Force (N)	Retention Force (N)
1	Straight	4	0.058 ± 0.035	0.034 ± 0.007
7	Straight	1	-	0.24
1	Barbed	3	0.275 ± 0.082	0.067 ± 0.01
7	Barbed	1	-	0.53

C. MNA Characterization

1) Mechanical: The AdminPatch, SLA MNA, and PEEK MNAs inserted easily into porcine ear skin with firm finger pressure (Fig. S13a-c). For the AdminPatch, the centermost microneedles tended to spring up from the skin when pressure was released, presumably due to a slight deformation or residual stress in the steel structure. Additionally, when applied to softer or slightly concave parts of the ear, the wide margins of the device tended to concentrate applied pressure at the edges rather than the center, further adding to the tendency for the microneedles to lift out of the skin. No microneedle was damaged by insertion into porcine ear, though, in thinner regions of the ear, it was possible with the longer PEEK microneedles to reach cartilage beneath the skin which blunted the tips.

Buckling, insertion, and retention force of laser-machined PEEK microneedles was measured; Fig. S13d-f shows representative force-time plots. Buckling force of single PEEK microneedles was 2.23 ± 0.19 N (mean ± SD, n = 6). Measured values of insertion and retention force into porcine ear are shown in Table II. Barbed tips had 4× larger insertion force and 2× the retention force. Retention force appeared to scale linearly with the number of needles in each array, *i.e.*, seven needles yielded a retention force ~ 7× that of one needle. Insertion force was not reported for seven-needle MNA insertions as the compound effects of multiple needles contacting the non-flat skin surface yielded multiple insertion events across a range of values.

2) In Vitro Sensing: Voltammetric titration with the MNA EAB sensors yielded strong SWV peaks and signal gain comparable to Au wire controls. Fig. S14a shows representative voltammograms from a Parylene-insulated MNA after smoothing and baseline adjustment. Fig. S14b shows signal gain from 1 μM to 1 mM for the AdminPatch sensor and PEEK MNA sensors which used laser-cut tape and conformally-coated Parylene insulation methods, with Au wire signal gain included for comparison.

Dual-target MNAs, functionalized with vancomycin- and phenylalanine-sensitive aptamers on separate WEs of the same array using a custom microfluidic fixture, were interrogated in concentrations of both targets. Each WE responded only

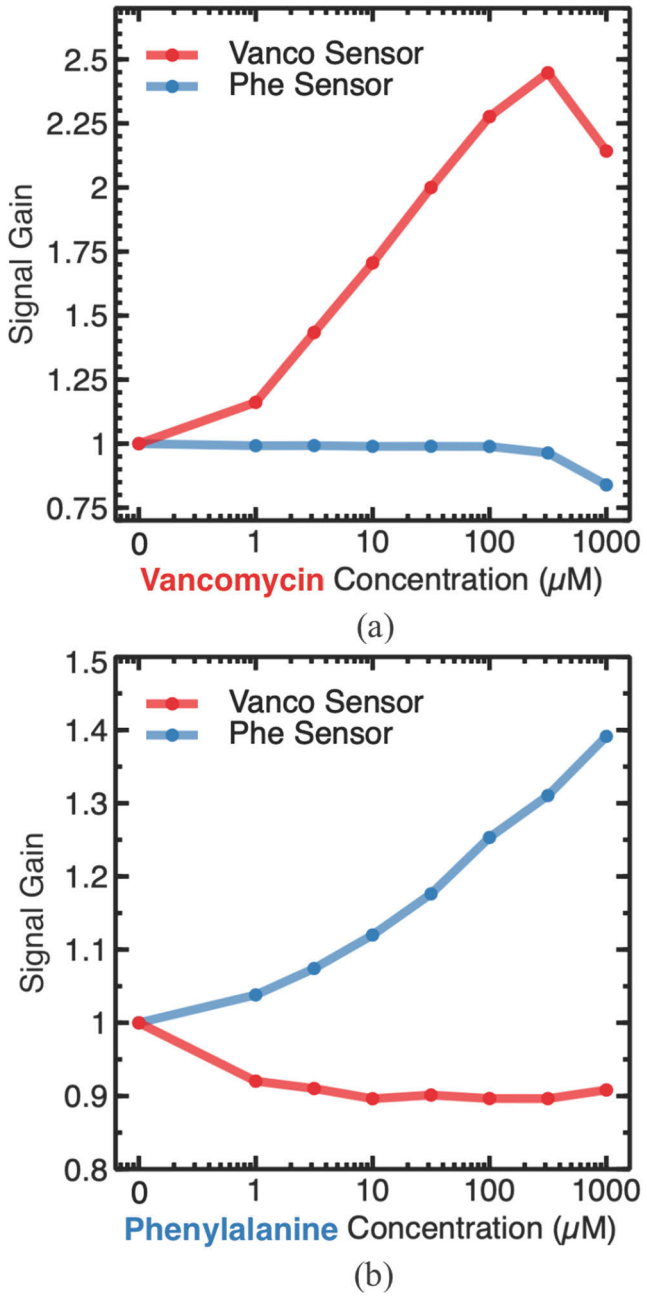


Fig. 8. Voltammetric titrations performed using independent sensors on the same MNA in (a) vancomycin (vanco) and (b) phenylalanine (phe). SWV was applied to both sensors simultaneously at 100 Hz in vancomycin and 300 Hz in phenylalanine as these are response frequencies characteristic of each aptamer.

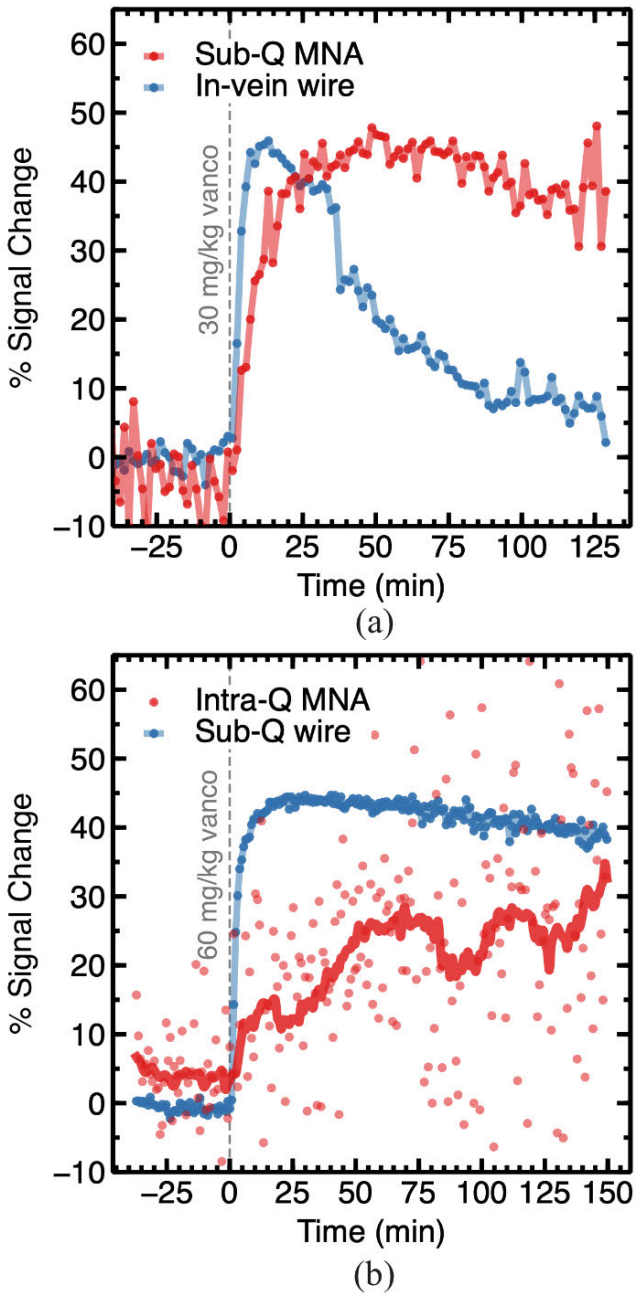


Fig. 9. EAB signals over time collected from anesthetized rats. (a) PEEK MNA surgically placed beneath the skin ("sub-Q") compared with an in-vein wire sensor. (b) PEEK MNA inserted into skin ("intra-Q") compared with a sub-Q wire sensor.

to its target molecule, confirming effective isolation of each electrode during incubation in the microfluidic fixture (Fig. 8).

3) In Vivo Sensing: We observed a response to intravenously infused vancomycin with PEEK MNA vancomycin sensors positioned sub- and intracutaneously in anesthetized rat. First, a PEEK MNA placed in the subcutaneous space was compared with a Au wire sensor in the jugular vein (Fig. 9a). The MNA response to vancomycin infusion exhibited a steep initial rise delayed from the in-vein sensor by ~2 min. The MNA gradually approached its peak and decayed by ~20% in the same period that the in-vein sensor nearly returned to baseline. Blood on the MNA upon removal indicated that measurements likely tracked concentrations in accumulating blood and interstitial fluid.

When comparing an intracutaneous PEEK MNA with a Au wire sensor placed subcutaneously, the Au wire exhibited a clear response to vancomycin infusion having a similar shape to subcutaneous measurements (Fig. 9b). The MNA's response suffered from noise, requiring application of a 19-point moving average. From this, a distinct rise from baseline corresponding to infusion was observed.

IV. Discussion

We investigated 17 materials as potential substrates for EAB sensor fabrication, testing first for Ti/Au adhesion then compatibility with EAB self-assembly and electrochemical processes. Seven of the materials exhibited less than 100% metal adhesion (PMMA, COC, MT4310 LCP, MT4350 LCP, FIT30 LCP, BIO, and HT200). Of the remaining ten, one failed during electrochemical cleaning (HTL) and two more did not yield useable signal (silicon and SS). Considering these results, we recommend the following materials as initial candidates for developing microfabricated EAB sensors: glass, PECVD SiO_2, Parylene C, PEEK, PEI, polystyrene, and LCP.

A Ti adhesion layer was effective for enhancing Au adhesion to some candidate materials. Despite little evidence from literature to suggest strong adhesion to polymers, excellent Ti/Au adhesion was observed on four thermoplastics and one SLA resin (though adhesion to the resin was lost upon exposure to sulfuric acid). These results address a knowledge gap on polymer substrates suitable for EAB sensing, [36], [37], [38], [39], [40], [41]. We hypothesize that thorough drying of the samples prior to metal deposition played a critical role in adhesion. Polymers are generally hygroscopic, and at the low pressures encountered during metal evaporation, any captured moisture is likely drawn to the surface, thereby affecting contact with and adhesion of incident metal atoms. Changing the metal deposition method may further increase the number of suitable substrate materials. For example, sputtering rather than evaporating may yield better Ti/Au adhesion on some materials. Incidental to the translation of EAB to thin film Au, we also identified an electrochemical cleaning protocol that was effective yet sufficiently gentle, as we found the protocol for solid Au wires too aggressive for thin films.

We found EAB sensing is dependent on having a non-conducting or adequately passivated surface. Sensors using Au deposited on conducting (stainless steel) or semiconducting (silicon) substrates did not result in any identifiable peak from the redox reporter, suggesting that the conductivity of the underlying substrate interfered with EAB sensing. Two mechanisms of interference are suggested. The first is that any defect in insulation or Au coverage provides an alternate current path from the conductive substrate to the solution which overpowers the aptamer signal. The second is that contact between Au and another metal in electrolytic solution produces a galvanic potential which interferes with self-assembly of the aptamer monolayer by altering surface charge distribution or inducing competing surface reactions. Because of these effects, insulators are preferred for producing EAB sensors that rely on thin film Au electrodes.

EAB sensors constructed using evaporated Au thin films can achieve equivalent signal gain performance compared to Au wire sensors. This allows EAB sensing to be extended to alternate interfaces, such as wearable microneedle formats.

Conformal Parylene C coatings could be applied to first passivate incompatible substrates before depositing Ti/Au. Therefore, MNAs using high-resolution 3D printed (SLA) polymer and stainless steel could be investigated as potential EAB sensing formats. An alternative method to form continuous conductive Au surfaces on the SLA needles is needed. Potential solutions include deposition via sputtering or electrodeposition for better sidewall coverage [22], [42], angled mounting, or smoothing of the surface via solvent evaporation.

The commercial AdminPatch drug delivery MNA supported EAB sensing, however, the pre-defined layout was restrictive and the spring-like quality of the stainless steel posed difficulties in maintaining needle engagement with skin, though this may be resolved by integration of an adhesive layer.

PEEK is an intriguing EAB sensor candidate as it is a high-performance thermoplastic possessing both physical strength and chemical resistance. The material has been employed in numerous orthopedic, spinal and cranial implants, including ones that are FDA-approved [43]. Furthermore, PEEK's combination of ductility and resilience allowed it to be shaped into a 3D MNA but not deform during handling or insertion.

The concept of cutting microneedle profiles into a planar substrate then bending them out-of-plane was previously demonstrated using sheet metal [44], [45], [46], [47]. To our knowledge, this is the first time this concept was used to achieve out-of-plane polymer microneedles, broadening its access to a different set of material characteristics.

Femtosecond laser machining resulted in conductive carbonized debris that could redeposit on MNA edges and interfere with sensor operation; thorough polishing with an abrasive cleaner and sonication was necessary to eliminate the debris. This polishing step was performed before characterization of the microneedle tip radii via SEM in Fig. S12 and since the abrasive likely blunted the tip, we may expect even sharper tips and lower insertion force if polishing can be avoided. A stream of compressed air near the machining site may prevent redeposition of debris. Li et al. achieved ablation of PEEK with almost no redeposited debris using a wavelength of 387 nm at which absorption was high; selecting this wavelength may also circumvent the issue [48].

Our initial microneedle designs were 800 μm long to terminate in the rat dermis with some extra length included to account for skin stretching and uneven skin surface (*e.g.*, unremoved hair). However, rat skin exhibited significant elasticity and toughness, resulting in dimpling, incomplete insertion, and ejection of microneedles after insertion pressure was removed. Increasing needle length to 1400 μm and inter-needle spacing (from 1 to 1.5 mm) improved insertion and retention. Adding barbs to the tip increased retention force 2×, suggesting room for additional design improvements.

The microneedles of our PEEK MNA were angled at ~65° from the substrate rather than 90°. Angled microneedles allow lateral force during insertion, using opposing tension in the skin to reach the insertion force threshold with less pressure applied to underlying tissues. Geometrically, angled microneedles may offer an increased surface area positioned in the targeted skin layer [49]. Compared to 90°, an angle of 65° theoretically provides an increase of ~10%.

Compared to fabrication of EAB electrodes in planar or wire formats, the 3D geometry of MNA patches required

development of non-traditional techniques for metal patterning, substrate insulation, and targeted incubation. The laser-cut shadow mask included anchoring structures for precise definition of multiple electrodes and contact pads. In the future, this may allow on-board implementation of the CE, RE, and multiple WE, though we explored up to two WE. Since the base of each microneedle shaft remains outside the dermis, polyimide tape insulation left a portion of each sensing area uninserted which may contribute to movement-related drift in behaving experiments. Parylene insulation, in contrast, allowed the entire sensing area to be inserted.

While a gold standard pharmacokinetic profile of intracutaneous/intradermal vancomycin does not exist, we hypothesize that the delayed and protracted intracutaneous MNA response (relative to the subcutaneous profile) resulted from slower diffusion and filtration through solid tissues of the skin. Assuming the noise level can be improved, we expect intracutaneous measurements from MNA EAB sensors like the PEEK MNA can inform multi-compartment pharmacokinetic models. This study has established groundwork for fabrication of other EAB sensor formats which can be tailored for implementation in other parts of the body.

V. Conclusion

We lay groundwork for a wider variety of EAB sensor formats by identifying new sensor construction materials towards realizing the broad and impactful applications of real-time in- and on-body molecular sensing. The candidate materials enabled consideration of a wide range of microfabrication methods to achieve various 2D and 3D formats. We applied our findings to produce and demonstrate different MNA-based EAB sensors at the benchtop and *in vivo*, including the first laser cut MNA EAB sensors. Implementing EAB sensing on microneedles served as a case study for its translation to new formats and aid in accelerating progress toward real-time in- and on-body molecular sensing.

Acknowledgment

The authors would like to thank Celanese, Polyplastics USA, and Boston Micro Fabrication for providing material samples; the staff of the USC John O'Brien Nanofabrication Laboratory for equipment maintenance and training; and the members of their laboratories at UCSB and USC, namely Lisa Fetter, Kaylyn Leung, James Yoo, Max Li, and Jenna Wen for their expertise and assistance.

Conflict of Interest

Kevin Plaxco serves on the advisory board and holds equity in a company that is commercializing EAB sensors.

References

[1] P. Dauphin-Ducharme et al., "Electrochemical aptamer-based sensors for improved therapeutic drug monitoring and high-precision, feedback-controlled drug delivery," *ACS Sensors*, vol. 4, no. 10, pp. 2832–2837, Oct. 2019, doi: 10.1021/acssensors.9b01616.

[2] C. Flatebo et al., "Efforts toward the continuous monitoring of molecular markers of performance," *J. Sci. Med. Sport*, vol. 26, pp. S46–S53, Jun. 2023, doi: 10.1016/j.jsams.2023.01.010.

[3] N. Arroyo-Currás, P. Dauphin-Ducharme, K. Scida, and J. L. Chávez, "From the beaker to the body: Translational challenges for electrochemical, aptamer-based sensors," *Anal. Methods*, vol. 12, no. 10, pp. 1288–1310, 2020, doi: 10.1039/d0ay00026d.

[4] R. D. Mishi, M. A. Stokes, C. A. Campbell, K. W. Plaxco, and S. L. Stocker, "Real-time monitoring of antibiotics in the critically ill using biosensors," *Antibiotics*, vol. 12, no. 10, p. 1478, Sep. 2023, doi: 10.3390/antibiotics12101478.

[5] N. Arroyo-Currás, J. Somerson, P. A. Vieira, K. L. Ploense, T. E. Kippin, and K. W. Plaxco, "Real-time measurement of small molecules directly in awake, ambulatory animals," *Proc. Nat. Acad. Sci. USA*, vol. 114, no. 4, pp. 645–650, Jan. 2017, doi: 10.1073/pnas.1613458114.

[6] A. Idili, J. Gerson, T. Kippin, and K. W. Plaxco, "Seconds-resolved, in situ measurements of plasma phenylalanine disposition kinetics in living rats," *Anal. Chem.*, vol. 93, no. 8, pp. 4023–4032, Mar. 2021.

[7] M. H. McDonough, S. L. Stocker, T. E. Kippin, W. Meiring, and K. W. Plaxco, "Using seconds-resolved pharmacokinetic datasets to assess pharmacokinetic models encompassing time-varying physiology," *Brit. J. Clin. Pharmacol.*, vol. 89, no. 9, pp. 2798–2812, Sep. 2023, doi: 10.1111/bcp.15756.

[8] J. Gerson et al., "High-precision monitoring of and feedback control over drug concentrations in the brains of freely moving rats," *Sci. Adv.*, vol. 9, no. 20, p. 3254, May 2023, doi: 10.1126/sciadv.adg3254.

[9] A. Chamorro-Garcia et al., "Real-time, seconds-resolved measurements of plasma methotrexate in situ in the living body," *ACS Sensors*, vol. 8, no. 1, pp. 150–157, Jan. 2023, doi: 10.1021/acssensors.2c01894.

[10] J. Kim, A. S. Campbell, B. E.-F. de Ávila, and J. Wang, "Wearable biosensors for healthcare monitoring," *Nature Biotechnol.*, vol. 37, no. 4, pp. 389–406, Apr. 2019, doi: 10.1038/s41587-019-0045-y.

[11] S. K. Garg, "Past, present, and future of continuous glucose monitors," *Diabetes Technol. Therapeutics*, vol. 25, no. S3, pp. 1–4, Jun. 2023, doi: 10.1089/dia.2023.0041.

[12] A. Idili et al., "Continuous monitoring of molecular biomarkers in microfluidic devices," *Prog. Mol. Biol. Translational Sci.*, pp. 295–333, Aug. 2021, doi: 10.1016/bs.pmbts.2021.07.027.

[13] H. Vaisocherová, E. Brynda, and J. Homola, "Functionalizable low-fouling coatings for label-free biosensing in complex biological media: Advances and applications," *Anal. Bioanal. Chem.*, vol. 407, no. 14, pp. 3927–3953, May 2015, doi: 10.1007/s00216-015-8606-5.

[14] R. S. Gaster et al., "Matrix-insensitive protein assays push the limits of biosensors in medicine," *Nature Med.*, vol. 15, no. 11, pp. 1327–1332, Nov. 2009, doi: 10.1038/nm.2032.

[15] P. Bayat et al., "SELEX methods on the road to protein targeting with nucleic acid aptamers," *Biochimie*, vol. 154, pp. 132–155, Nov. 2018, doi: 10.1016/j.biochi.2018.09.001.

[16] A. A. Lubin and K. W. Plaxco, "Folding-based electrochemical biosensors: The case for responsive nucleic acid architectures," *Accounts Chem. Res.*, vol. 43, no. 4, pp. 496–505, Apr. 2010, doi: 10.1021/ar900165x.

[17] A. I. Muñoz-Martínez, O. I. González Peña, J. Colomer-Farrarons, J. M. Rodríguez-Delgado, A. Ávila-Ortega, and G. Dieck-Assad, "Electrochemical instrumentation of an embedded potentiostat system (EPS) for a programmable-system-on-a-chip," *Sensors*, vol. 18, no. 12, p. 4490, Dec. 2018, doi: 10.3390/s18124490.

[18] Y. Xiao, A. A. Lubin, A. J. Heeger, and K. W. Plaxco, "Label-Free electronic detection of thrombin in blood serum by using an aptamer-based sensor," *Angew. Chem. Int. Ed.*, vol. 44, no. 34, pp. 5456–5459, Aug. 2005, doi: 10.1002/anie.200500989.

[19] J. Gerson et al., "A high-precision view of intercompartmental drug transport via simultaneous, seconds-resolved, in situ measurements in the vein and brain," *Brit. J. Pharmacol.*, vol. 181, no. 20, pp. 3869–3885, Oct. 2024, doi: 10.1111/bph.16471.

[20] J.-W. Seo, K. Fu, S. Correa, M. Eisenstein, E. A. Appel, and H. T. Soh, "Real-time monitoring of drug pharmacokinetics within tumor tissue in live animals," *Sci. Adv.*, vol. 8, no. 1, p. 2901, Jan. 2022, doi: 10.1126/sciadv.abk2901.

[21] B. S. Ferguson et al., "Real-time, aptamer-based tracking of circulating therapeutic agents in living animals," *Sci. Translational Med.*, vol. 5, no. 213, Nov. 2013, Art. no. 213ra165, doi: 10.1126/scitranslmed.3007095.

[22] M. Reynoso et al., "3D-printed, aptamer-based microneedle sensor arrays using magnetic placement on live rats for pharmacokinetic measurements in interstitial fluid," *Biosensors Bioelectron.*, vol. 244, Jan. 2024, Art. no. 115802, doi: 10.1016/j.bios.2023.115802.

[23] Y. Wu et al., "Microneedle aptamer-based sensors for continuous, real-time therapeutic drug monitoring," *Anal. Chem.*, vol. 94, no. 23, pp. 8335–8345, Jun. 2022, doi: 10.1021/acs.analchem.2c00829.

[24] S. Lin et al., "Wearable microneedle-based electrochemical aptamer biosensing for precision dosing of drugs with narrow therapeutic windows," *Sci. Adv.*, vol. 8, no. 38, p. 4539, Sep. 2022, doi: 10.1126/sciadv.abq4539.
[25] F. V. Oberhaus, D. Frense, and D. Beckmann, "Immobilization techniques for aptamers on gold electrodes for the electrochemical detection of proteins: A review," *Biosensors*, vol. 10, no. 5, p. 45, Apr. 2020, doi: 10.3390/bios10050045.
[26] K. Xu, X. Meshik, B. M. Nichols, E. Zakar, M. Dutta, and M. A. Stroscio, "Graphene- and aptamer-based electrochemical biosensor," *Nanotechnology*, vol. 25, no. 20, Apr. 2014, Art. no. 205501, doi: 10.1088/0957-4484/25/20/205501.
[27] Z. M. Karazan, M. Roushani, S. J. Hoseini, and M. Nasibipour, "Designing an electrochemical aptasensor based on a microstructure porous-covalent organic polymer for the determination of 2,4,6-trinitrotoluen in water and soil samples," *Microchemical J.*, vol. 204, Sep. 2024, Art. no. 110975, doi: 10.1016/j.microc.2024.110975.
[28] F. Hamdi, M. Roushani, M. Nasibipour, and S. J. Hoseini, "Aptasensor based on high surface area covalent organic framework for simple and ultrasensitive detection of sarcosine in the diagnosis of prostate cancer," *Analytica Chim. Acta*, vol. 1291, Feb. 2024, Art. no. 342235, doi: 10.1016/j.aca.2024.342235.
[29] L. Ferrer Pascual, E. Gustafsson, J. Siitonen, V. Durairaj, and T. Laurila, "Challenges in aptamer-based sensor development using carbon nanotube networks," *Sensors Diag.*, vol. 3, no. 12, pp. 1935–1946, 2024, doi: 10.1039/d4sd00250d.
[30] *Test Methods for Rating Adhesion By Tape Test*, ASTM International, West Conshohocken, PA, USA, 2023.
[31] C. A. Canaria et al., "Formation and removal of alkylthiolate self-assembled monolayers on gold in aqueous solutions," *Lab a Chip*, vol. 6, no. 2, p. 289, 2006, doi: 10.1039/b510661c.
[32] *Thin-Film (micro)Electrodes-Surface Cleaning & Activation*. Accessed: Jun. 1, 2023. [Online]. Available: https://www.micruxfluidic.com/archivos/MicruX_thin-film_electrodes_cleaning.pdf
[33] Y. Xiao, R. Y. Lai, and K. W. Plaxco, "Preparation of electrode-immobilized, redox-modified oligonucleotides for electrochemical DNA and aptamer-based sensing," *Nature Protocols*, vol. 2, no. 11, pp. 2875–2880, Nov. 2007, doi: 10.1038/nprot.2007.413.
[34] P. Dauphin-Ducharme, K. L. Ploense, N. Arroyo-Currás, T. E. Kippin, and K. W. Plaxco, "Electrochemical aptamer-based sensors: A platform approach to high-frequency molecular monitoring in situ in the living body," in *Proc. Biomed. Eng. Technol.*, vol. 2393, 2021, pp. 479–492, doi: 10.1007/978-1-0716-1803-5_25.
[35] U. Jacobi et al., "Porcine ear skin: An in vitro model for human skin," *Skin Res. Technol.*, vol. 13, no. 1, pp. 19–24, Feb. 2007, doi: 10.1111/j.1600-0846.2006.00179.x.
[36] S. Sharma, A. Saeed, C. Johnson, N. Gadegaard, and A. E. Cass, "Rapid, low cost prototyping of transdermal devices for personal healthcare monitoring," *Sens. Bio-Sensing Res.*, vol. 13, pp. 104–108, Apr. 2017, doi: 10.1016/j.sbsr.2016.10.004.
[37] R. Melentiev, A. Yudhanto, R. Tao, T. Vuchkov, and G. Lubineau, "Metallization of polymers and composites: State-of-the-art approaches," *Mater. Design*, vol. 221, Sep. 2022, Art. no. 110958, doi: 10.1016/j.matdes.2022.110958.
[38] C.-M. Han et al., "The electron beam deposition of titanium on polyetheretherketone (PEEK) and the resulting enhanced biological properties," *Biomaterials*, vol. 31, no. 13, pp. 3465–3470, May 2010, doi: 10.1016/j.biomaterials.2009.12.030.
[39] A. Reznickova, Z. Novotna, S. Rimpelova, J. Siegel, and V. Svorcik, "Engineering PEEK bioactivity: Effect of plasma and gold sputtered interface," *Mater. Today, Proc.*, vol. 3, no. 2, pp. 115–124, 2016, doi: 10.1016/j.matpr.2016.01.036.
[40] Z. Novotná et al., "Tuning surface chemistry of polyetheretherketone by gold coating and plasma treatment," *Nanosc. Res. Lett.*, vol. 12, no. 1, p. 424, Dec. 2017, doi: 10.1186/s11671-017-2182-x.
[41] R. Kukla, D. Hofmann, G. Ickes, and U. Patz, "Sputter metallization of plastic parts in a just-in-time coater," *Surf. Coatings Technol.*, vols. 74–75, pp. 648–653, Oct. 1995, doi: 10.1016/0257-8972(95)08266-2.
[42] Y. Liu, Q. Yu, X. Luo, L. Yang, and Y. Cui, "Continuous monitoring of diabetes with an integrated microneedle biosensing device through 3D printing," *Microsystems Nanoengineering*, vol. 7, no. 1, p. 75, Sep. 2021, doi: 10.1038/s41378-021-00302-w.
[43] J. Graham and J. Peck, "FDA regulation of PEEK implants," in *PEEK Biomaterials Handbook*. Amsterdam, The Netherlands: Elsevier, 2019, pp. 431–445, doi: 10.1016/B978-0-12-812524-3.00026-0.
[44] *AdminPatch 0900 Microneedle Array — AdminMed*. Accessed: Jan. 4, 2024. [Online]. Available: http://www.adminmed.com/array0900
[45] W. Martanto, S. P. Davis, N. R. Holiday, J. Wang, H. S. Gill, and M. R. Prausnitz, "Transdermal delivery of insulin using microneedles in vivo," *Pharmaceutical Res.*, vol. 21, no. 6, pp. 947–952, Jun. 2004, doi: 10.1023/b:pham.0000029282.44140.2e.
[46] H. S. Gill and M. R. Prausnitz, "Coated microneedles for transdermal delivery," *J. Controlled Release*, vol. 117, no. 2, pp. 227–237, Feb. 2007, doi: 10.1016/j.jconrel.2006.10.017.
[47] S. J. Lee, H. S. Yoon, X. Xuan, J. Y. Park, S.-J. Paik, and M. G. Allen, "A patch type non-enzymatic biosensor based on 3D SUS micro-needle electrode array for minimally invasive continuous glucose monitoring," *Sens. Actuators B, Chem.*, vol. 222, pp. 1144–1151, Jan. 2016, doi: 10.1016/j.snb.2015.08.013.
[48] Q. Li et al., "A study on ultrafast laser micromachining and optical properties of amorphous polyether(ether)ketone (PEEK) films," *Proc. CIRP*, vol. 94, pp. 840–845, Sep. 2020, doi: 10.1016/j.procir.2020.09.113.
[49] R. Murty, A. Sankaranarayanan, I. I. Bowland, J. Mena-Lapaix, and M. R. Prausnitz, "Angled insertion of microneedles for targeted antigen delivery to the epidermis," *Pharmaceutics*, vol. 14, no. 2, p. 347, Feb. 2022, doi: 10.3390/pharmaceutics14020347.



Christopher E. Larson received the B.M. degree in music composition from Biola University, La Mirada, CA, USA, in 2009, and the B.S. and Ph.D. degrees in biomedical engineering from the University of Southern California, Los Angeles, CA, USA, in 2015 and 2025, respectively. His research focuses on polymer microfabrication and laser micromachining for implantable and wearable biomedical interfaces.



Emmanuel Ramirez received the B.S. degree in mechanical engineering from California State University Los Angeles (CSULA) in 2022. He is currently pursuing the Ph.D. degree in biomedical engineering with the University of Southern California (USC) under the guidance of Dr. E. Meng. His research interests include wearable and passive sensing of biomarkers.



Chelsea N. Brown received the Ph.D. degree in behavioral neuroscience from the University of California, Santa Barbara (UCSB) in 2022, researching signaling mechanisms in the brain's reward circuitry that underlie methamphetamine abuse using mouse models. She is currently a Post-Doctoral Researcher with the Kippin/Plaxco Laboratory, UCSB. Her current research interests include developing animal models to adapt biosensors for translational and clinical applications, understanding pharmacokinetics throughout the body using high-resolution data from multiple physiological compartments, and investigating individual differences in drug responses to minimize off-target effects and maintain therapeutic efficacy.



Kayla (Yuting) Wang received the B.S. degree in psychology from the University of Washington, Seattle, in 2019. She is currently pursuing the Ph.D. degree with the University of California, Santa Barbara (UCSB) under Dr. Tod Kippin. Her research interests include exploring the utility of electrochemical aptamer-based (EAB) sensors to access the role of pharmacokinetics in animal models for clinical applications.

Tod Kippin , photograph and biography not available at the time of publication.

Kevin Plaxco , photograph and biography not available at the time of publication.



Ellis Meng (Fellow, IEEE) received the B.S. degree in engineering and applied science and the M.S. and Ph.D. degrees in electrical engineering from California Institute of Technology (Caltech), Pasadena, in 1997, 1998, and 2003, respectively. Since 2004, she has been with the University of Southern California, Los Angeles, where she is currently the Shelly and Ofer Nemirovsky Chair of Convergent Biosciences and a Professor in biomedical engineering and in electrical and computer engineering. She is also the Vice Dean of Technology Innovation and Entrepreneurship. Her research interests include bioMEMS, implantable biomedical microdevices, microfluidics, multimodality integrated microsystems, and packaging. She is a fellow of ASME, BMES, AIMBE, and NAI. Her honors include the NSF CAREER Award, the Wallace H. Coulter Foundation Early Career Award, the 2009 TR35 Young Innovator Under 35, the Viterbi Early Career Chair, the ASEE Curtis W. McGraw Research Award, the 2018 IEEE Engineering in Medicine and Biology Society Technical Achievement Award, and the 2019 IEEE Sensors Council Technical Achievement Award.